scientific reports

Check for updates

OPEN

Nanostructural and nanomechanical alterations of photosensitized lipid membranes due to light induced formation of reactive oxygen species

Ádám Zolcsák[1], Bálint Kiss[1], Tamás Bozó[1], Judit Somkuti[1], István Vona[2], Miklós Kellermayer[1] & Levente Herenyi[1]✉

Photosensitization has a wide range of applications in vastly distant fields. Three key components must be present at the same time to trigger the related photodynamic effect: light, the photosensitizer (PS) and oxygen. Irradiating the sensitizer leads to the formation of reactive oxygen species (ROS). Since PSs are accumulated preferably in lipid membranes, the study of photoinduced damage to membrane lipids can greatly increase our understanding of the effect of ROS on membranes in pathological as well as therapeutic conditions. We aimed to characterize the topographical and nanomechanical changes in supported lipid bilayers (SLBs) evoked by light-induced ROS formation. SLBs were prepared on mica surfaces by deposition of liposomes containing unsaturated lipid components. Topographical changes of SLBs were imaged by atomic force microscopy (AFM), and ROS-induced nanomechanical alterations of the membranes were assessed by AFM force measurements. To shed light on chemical alterations of the membrane constituents, infrared spectra were recorded. In the AFM images of porphyrin-containing membranes nanoscopic, bilayer-spanning holes were detected after irradiation. The measured rupture forces increased as a result of irradiation. These phenomena did not occur in membranes lacking unsaturated lipid components, emphasizing their role in ROS-mediated disruption confirmed by infrared spectroscopy results.

Photosensitization is the ability to induce a toxic reaction to light in a living system. Photodynamic therapy (PDT) has been the leading application of photosensitization, the basis of which is a dye molecule. The photosensitizer (PS), usually a porphyrin derivative, is excited by light which causes a photochemical reaction leading to the formation of lethal cytotoxic agents. The limited lifetime of the generated agents localizes most of the harmful alterations of cell components in the region where the PS is accumulated. Porphyrin analog PSs can accumulate in tumors or tissues where neovascularization is taking place, which enables the passive targeting of the desired cells. PS can also be conjugated to specific carrier molecules to provide site-selective accumulation1[1]. Following the accumulation of PS targeted irradiation can serve as a highly selective treatment, hence PDT is most often utilized in oncology in the eradication of tumorous tissue. PDT is a potential therapeutic modality for other nonmalignant diseases as well, such as age-related macular degeneration (AMD)[1], psoriasis[2], or atherosclerosis[3]. Recently photodynamic inactivation (PDI), a promising antimicrobial method has gained significant interest. The underlying principles of PDI are very similar to PDT, in this case, pathogens which have accumulated the PSs can be eliminated by irradiation[4]. Despite the diverse applications of the photodynamic action, their foundation is the same.

The molecular actions of PDT are triggered by the illumination of the administered PS by light of the appropriate wavelength that excites the molecule from its ground state (S0) to an excited singlet state (S1). This excited state can release excess energy through fluorescence or non-radiative decay. A fraction of the S1 state molecules can transit into an excited triplet state (T1). A molecule in this T1 state either loses its energy through phosphorescence or transfers it to other molecules by collision. There are two distinct types of reactions: *(a)* type I reactions occur when the PS in its excited T1 state transfers an electron or a hydrogen atom to form radical

[1]Department of Biophysics and Radiation Biology, Semmelweis University, Budapest, Hungary. [2]MTA-ELTE "Momentum" Integrable Quantum Dynamics Research Group, Eötvös Loránd University, Budapest, Hungary. ✉email: herenyi.levente@semmelweis.hu

species, or *(b)* during type II reactions the excited PS in the T1 state directly interacts with ground state molecular oxygen to form singlet oxygen. The products of these reactions are referred to as reactive oxygen species (ROS). ROS are responsible for tissue damage in various physiological and pathological conditions. Nascent ROS generated through photosensitization, especially type II reaction products, have a limited effective range due to their short lifetime[5]. This confines the deleterious effects of the generated ROS into a well-localized radius. The effective range of the produced singlet oxygen is in the nanometer order meaning that the cell component being affected largely depends on the subcellular location of the PS[6]. For sufficient accumulation of PSs in the target tissue high lipophilicity is necessary. This in turn can regulate the subcellular location of these molecules favoring various membrane-based structures such as the plasma membrane, the mitochondria, the lysosome and other cell organelles. Generally, the membrane binding efficiency of the PS correlates with its photodynamic efficiency[7]. Light-induced ROS production can lead to membrane damage and hole formation, which may lead to the leakage of ions and molecules[8–10]. Thus, membranes are a major target for photoinduced cell disruption.

In previous works of our research group, we determined the locations and compared the binding parameters of two different porphyrin PSs, namely mesoporphyrin IX dihydrochloride (MPCl) and mesoporphyrin IX dimethyl ester (MPE) in the membranes of small unilamellar vesicles (SUV) made from various saturated phosphatidylcholines[11,12]. Furthermore, we demonstrated the vesicle-disrupting capability of the studied PSs as direct evidence of membrane destruction by applying unsaturated phosphatidylcholines as membrane components[13]. We found that although the irradiation of MPCL-containing samples yielded more ROS observed, SUV disruption was less pronounced compared to the MPE-containing samples. This discrepancy between membrane disruption is due to the differing location of the two photosensitizers.

In the present work, our goal was to investigate the light-induced topographical alterations of PS-containing phospholipid membranes by using high-resolution atomic force microscopy (AFM) imaging. Furthermore, we aimed to assess ROS formation induced alterations of membrane mechanics and explore the possible molecular processes behind the observed phenomena.

Materials and methods

Chemicals

1,2-dipalmitoyl-sn-glycerol-phosphocholine (DPPC) and 1,2-dioleoyl-sn-glycerol-phosphocholine (DOPC) were purchased from Avanti Polar Lipids Inc. Dimethyl 7,12-diethyl-3,8,13,17-tetramethyl-21 H,23 H-porphine-2,18-dipropionate (MPE) was acquired from Frontier Scientific, Inc., Logan, UT. Whatman® Nucleopore track-etched polycarbonate membrane filters with pore diameter 400, 100, 50 nm were purchased from Merck KGaA, Darmstadt, Germany. Argon 5.0 and Nitrogen 5.0 gases were from Linde Gáz Magyarország Zrt. (Budapest, Hungary). Water was purified with a Milli-Q Integral 3 Water Production Unit (Merck Millipore, Billerica, MA). Round mica sheets were from Ted Pella Inc. (Redding, CA). Glucose oxidase (GO) from Aspergillus Niger and Catalase (C) from bovine liver were purchased from Merck KGaA, Darmstadt, Germany. All other chemicals were from Merck Ltd. (Budapest, Hungary).

Preparation of small unilamellar vesicles (SUVs)

SUVs were formed by the lipid extrusion method. 10 mg lipid either DPPC or DPPC-DOPC in 70:30 m/m% was dissolved in 200 µl chloroform in a clean glass vial, then the organic solvent was evaporated under a steady stream of argon gas. Subsequently, the glass tubes were kept in a vacuum-desiccator ($p < 20$ mbar) at least for one night to remove solvent traces. The prepared lipid films were hydrated at 55 °C by adding phosphate-buffered saline (PBS) (20 mM phosphate, 137 mM NaCl, pH 7.4) in increments of 200 µl five times with vigorous shaking resulting in a lipid solution with 1 mg/ml concentration. The resulting liposome suspension was extruded through polycarbonate membranes using an Avanti Mini Extruder at 55 °C to produce small unilamellar vesicles. The initial extrusion happened through a 400 nm pore size filter 15 times, followed by 15 subsequent extrusions through a 100 nm pore size filter.

Preparation of supported lipid bilayers (SLBs)

To allow the formation of a continuous SLB, we incubated 100 µl of the freshly prepared SUVs diluted by PBS to 0.08 mg/ml lipid concentration on a freshly cleaved mica surface for 30 min. To allow the lipids to coat the whole mica surface after incubation, the sample was heated to 60 °C at a rate of 1 °C/s for 15 min with the environmental module of the AFM. After heating the sample was cooled back to 25 °C at a rate of 0.1 °C/s. Finally, the sample surface was rinsed ten times with 100 µl PBS to remove any non-adhered vesicles from the surface.

Samples

SLBs containing both DPPC and DOPC were prepared from the lipids in a 70:30 mass ratio with the vesicle fusion method. Our photosensitized membranes contained MPE in saturation concentration[11]. We incubated a 30 m/m% H_2O_2 solution on the surface for 15 min then we washed it with PBS buffer. When experiments were performed in oxygen-deficient conditions to eliminate the dissolved oxygen from our buffer, we added glucose oxidase (GO) and catalase (C) enzymes to our buffer in 0.625 mg/ml GO and 0.04 mg/ml C concentrations. For these experiments, the DPPC-DOPC-MPE SLBs were prepared in 12.5 m/m% glucose solution with a 57 mM phosphate buffer to ensure that the added enzyme system would not alter the pH of the sample.

Irradiation

Irradiation of the SLB surface was carried out with the built-in quasi-white light LED light source of the AFM, which enabled continuous illumination during AFM imaging.

AFM imaging

SLB surfaces were scanned in non-contact mode. AFM imaging was carried out under liquid, in 100 µl of 20 mM PBS unless otherwise stated. We used silicon nitride AFM cantilevers (BL-AC40TS-C2, OLYMPUS, Japan) with ~8 nm nominal tip radius and ~90 pN/nm as nominal stiffness mounted in an Asylum Research Cypher ES instrument (Asylum Research, Santa Barbara, CA). The cantilevers were oscillated near their resonance frequencies by applying photothermal excitation utilizing BlueDrive technology. Scanning rates were typically between 1 and 2 Hz. The images were collected at 25 ± 0.1 °C. Image acquisition with the above-specified settings took ca. 4 min.

Force measurements

Force-distance curves were collected from preselected areas in the form of 32 × 32 force maps. The areas were chosen from pre-scanned AFM images. Due to the significantly different nanomechanical properties of the liquid-ordered and liquid-disordered states, each force map was recorded from within a single phase. The acquired force curves were collected from the liquid-ordered domains as the detected changes were present in these domains during the AFM imaging.

The average acquisition rate of force-distance curves was 1.6 Hz. Force-distance curves were acquired by pressing the tip of the cantilever against the sample with a constant 1 µm/s velocity until a preset maximal force typically between 1 and 8 nN was reached. Force-distance curves were median-filtered and analyzed using a custom-written algorithm[14] to acquire the breakthrough forces and the corresponding membrane rupture thicknesses. During our evaluation, we only analyzed rupture events that corresponded to forces higher than 0.5 nN and had a rupture thickness greater than 0.1 nm.

FTIR spectrometry

FTIR spectra were measured with a Bruker Vertex 80v spectrometer (Bruker Corp. Billerica, MA, USA) combined with a high sensitivity photoconductive mercury cadmium telluride detector with an attenuated total reflectance (ATR) module. 256 spectra were averaged at a 2 cm^{-1} resolution. Infrared spectra were collected between 400 cm^{-1} and 4000 cm^{-1}. To reduce the vibrational peaks of water we applied a steady stream of nitrogen to desiccate our samples, before each measurement.

Data processing

AFM image post processing and force curve analysis were performed in the AFM driving software (Igor Pro 7, AR 13.16.100). Distributions were analyzed using the "Gaussian multipeaks fit" and "nonlinear curve fit" routines from Origin 7 software (OriginLab Corporation). For image processing Fiji, ImageJ (doi:https://doi.org/10.1038/nmeth.2089) was used. Determination of the surface tension and line tension was carried out based on the analytical solution of the integral provided by Robinson et al.[15]. The fitting was carried out in Jupyter notebook with the SciPy (1.7.3) curvefit function.

Results

ROS induces hole formation in DOPC-DPPC membranes

To assess ROS-induced alterations in the membrane structure, we performed AFM imaging on SLBs. The SLBs were either photosensitized and then exposed to irradiation resulting in the generation of in situ generated ROS or H_2O_2 that was added directly to the system. Before irradiation, DPPC-DOPC-MPE membranes exhibited two distinct separated phases (Fig. 1a). The phase depicted with yellowish tones protruded from the other phase represented as the orange background by a height difference of ca. 2 nm. Both phases were quite smooth with no visible discontinuity within them. According to the usual classification, we identified the lower region as the liquid-disordered domain enriched in DOPC, and the higher areas as the liquid-ordered, DPPC-enriched domains[16]. The height of the liquid-disordered domain was set as the reference height for the images, as this domain occupies most of the surface.

Upon irradiation, membrane holes appeared in the photosensitized SLB (Fig. 1b). Hole formation was more pronounced in the liquid-ordered domains. The presence of the holes indicates compromised SLB integrity. To test if hole formation can be induced by the direct addition of ROS, we added H_2O_2 to DPPC-DOPC SLBs. First, a DPPC-DOPC SLB was imaged, then H_2O_2 was applied and subsequently imaged. Prior to H_2O_2 treatment, continuous, confluent, two-phase bearing SLB surface was observed (Fig. 1c), similar to that in the case of the DPPC-DOPC-MPE sample prior to irradiation (Fig. 1a). Then, distinct holes appeared in SLBs upon H_2O_2 treatment (Fig. 1d), similarly to the sensitized bilayers upon irradiation (Fig. 1b).

To investigate the role of unsaturated lipid components in the structural changes, we prepared SLBs from SUVs that only consisted of DPPC, and added MPE to the sample in saturation concentration (DPPC-MPE sample). The topography of these membranes remained confluent and unchanged following irradiation similar to Fig. 1a. DPPC-DOPC samples without MPE were also investigated and the mapped surfaces remained unchanged after irradiation.

Evolution of membrane holes

To study the dynamics of membrane hole formation, a sequence of images was collected during continuous irradiation. Eight consecutive frames are presented in Fig. 2a.

Already at the first frame holes are observable, indicating that light-induced ROS formation and the consequent hole formation is a relatively quick process. The first holes are formed well within the time frame (4 min) necessary to record an AFM image with our settings. At the timescale of a few minutes, the following phenomena were observable: first holes with small diameters appeared in a fast initial burst, followed by the

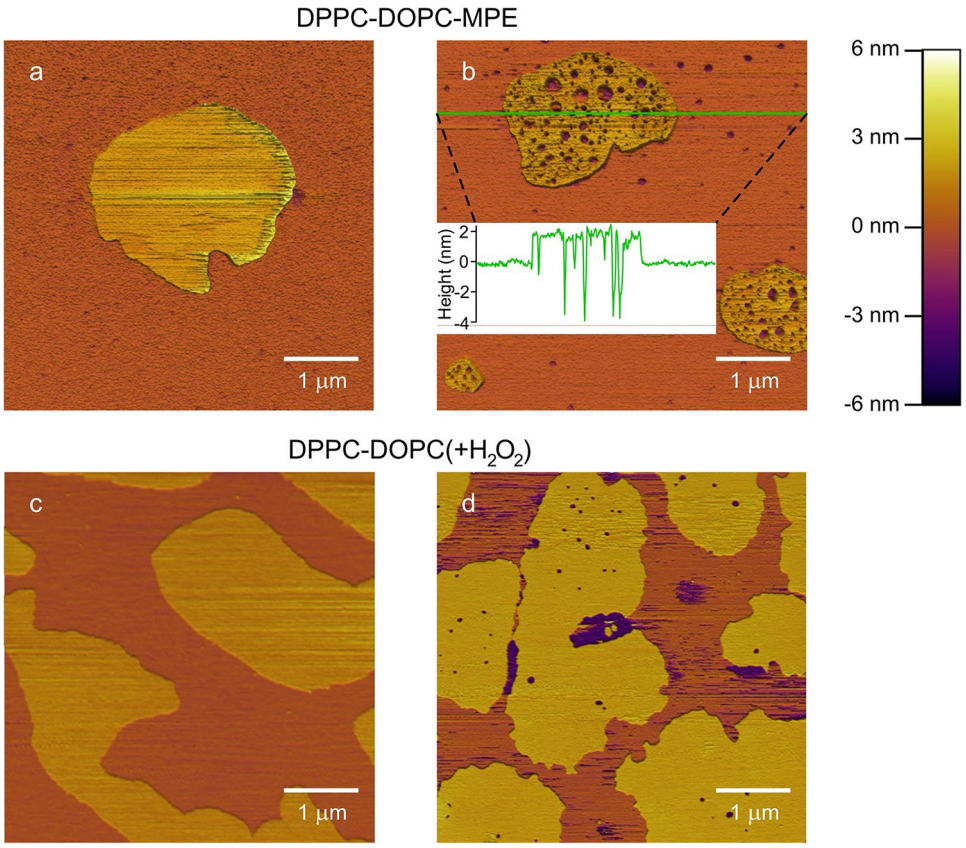

Fig. 1. Effect of ROS on SLBs. 5×5 µm AFM height-contrast images. The color scale for height is given in the upper right corner. Orange and yellow tones mark the liquid-disordered and liquid-ordered domains, respectively. (**a**) DPPC-DOPC-MPE SLB before and (**b**) after irradiation: the membrane is covered in nanoscale holes. The holes are more distinct and numerous in the liquid-ordered domains. The inserted height section profile shows the height along the green line. (**c**) DPPC-DOPC SLB before and d) after adding H_2O_2 to it. Membrane holes alike to holes in photosensitized membranes were observed.

increase of the average hole diameter paired with a decrease in the total number of holes. The area of the liquid-ordered phase steadily increased during the observation time.

The vast majority of holes kept their position throughout the imaging as displayed in Fig. 2a. The fate of the holes was rather diverse on the individual hole level: growth and subsequent shrinking, fusion, and disappearance of holes were all observed during the image acquisition. To characterize the dynamics of the observed holes, we displayed the distribution of hole diameters for each frame in Fig. 2b. The area of the holes was determined by particle analysis in ImageJ after proper thresholding for the holes (see the 8th frame in Fig. 2a). Each hole was assigned the area of a circle equal to the area of the hole, as the shape of some of the holes deviated from a perfect circle. Due to the uncertainties of the evaluation process, we used a relative scale to display the hole diameters, the estimated average hole diameters were in the tens of nanometers range.

For better visualization of cumulative distributions, we fitted them with Gaussian curves and determined the characteristic parameters: expected hole diameter (c means the center), width (w), and height (h), which is equal to the total number of holes detected. A few membrane discontinuities were already present on the 1st frame. On the 3rd and 4th frame we can observe the sudden appearance of numerous light-induced holes, and due to this there is a slight decrease in the c parameter at the 3rd frame as the freshly appearing holes are small. On the 4th frame the number of present holes peaks, while the spread of the holes is minimal. Between the 3rd and 6th frame the total area covered by the holes increases linearly, then it slightly decreases (see Fig. 2c). Although many different processes can influence the diameter of individual holes highlighted with circles on Fig. 2a, the average hole diameter (parameter c) steadily increases from the 3rd frame forward.

Characterization of nanomechanical properties of irradiated bilayers

The mechanical properties of bilayers are sensitive to their phase, composition and chemical environment. Thus, measuring membrane mechanical parameters can serve as a sensitive indicator of alterations in the intermolecular interactions within the membrane. For this purpose, force measurements were carried out with AFM. In these experiments, SLBs were compressed and ultimately punctured by the tip of the AFM. A representative force-distance curve of a DPPC-DOPC SLB is displayed in Fig. 3.

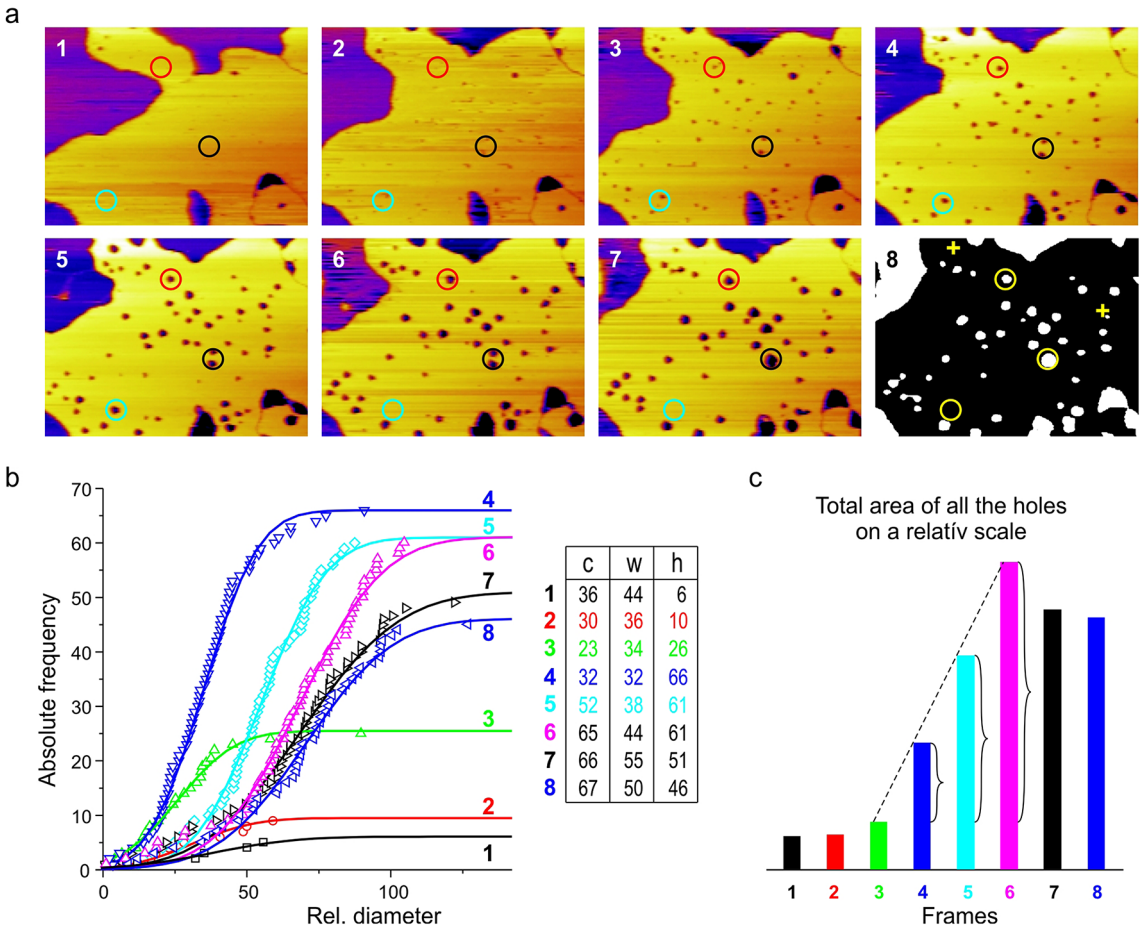

	c	w	h
1	36	44	6
2	30	36	10
3	23	34	26
4	32	32	66
5	52	38	61
6	65	44	61
7	66	55	51
8	67	50	46

Fig. 2. Evolution of membrane holes. (**a**) A chronological sequence of height-contrast AFM images were taken of the same region of DPPC-DOPC-MPE (ca. 2.35 × 1.75 µm) SLB during continuous irradiation. The frame rate is ca. 4 min. Liquid-ordered domains are displayed in yellow the holes appear as dark spots. Appearance, expansion or fusion, reduction or total disappearance of holes is observable (see the different colored circles). The 8th frame shows the image transformed by ImageJ where the "disappeared" holes are marked with yellow crosses. (**b**) The cumulative distributions of relative hole diameters for the series of frames are presented, fitted with the Gaussian curves. The fit parameters are given in the table. c stands for the center w for width and h stands for height. (**c**) The total area of the holes for each frame. Curly brackets show the linear proportion of increments in the total area covered by holes.

When the tip is away from the surface, there is no measurable force acting on the cantilever resulting in an initial horizontal section ($F \approx 0$ nN). As soon as the probe comes into contact with the bilayer surface, force starts to increase immediately until the bilayer yields at a certain load. The load where the membrane yields is called the rupture force. Since at this point the tip pierces through the bilayer, the corresponding segment of the force-distance curve is horizontal. These rupture forces are characteristic of the mechanical state of the bilayer. Depending on the state of the bilayer (e.g. coupling between the bilayer's two leaflets), tip penetration can happen in one or two steps. After the tip penetrates the bilayer, it is pressed against the hard substrate surface leading to a sharp increase in the recorded force values.

In Fig. 3 the displayed force-distance curve contains two distinct rupture events, therefore it can be characterized by two rupture forces (F_1, F_2) and corresponding rupture thicknesses (x_1, x_2). The rupture thicknesses are defined as the distance between the point where the bilayer ruptures and the point where the force starts to rise again. In several cases, the recorded force-distance curves displayed two events, while in some cases, we could identify only one. Moreover, the bilayer can also be ruptured in just one step, we call this event a *complete rupture*. Although F_2 is always larger than F_1 in the same force-distance curve (see Fig. 3), the distribution of F_2 overlaps with some recorded F_1 values if we consider the set of forces. All force measurements were recorded from liquid-ordered lipid regions.

Irradiation does not alter membrane mechanics in the absence of MPE

To assess whether light irradiation without PSs affects the mechanical properties of the studied bilayers on the experimental timescale, we created DPPC-DOPC SLBs without MPE as a control for our measurements. The DPPC-DOPC SLB did not show any topographical changes due to irradiation. However, this does not exclude

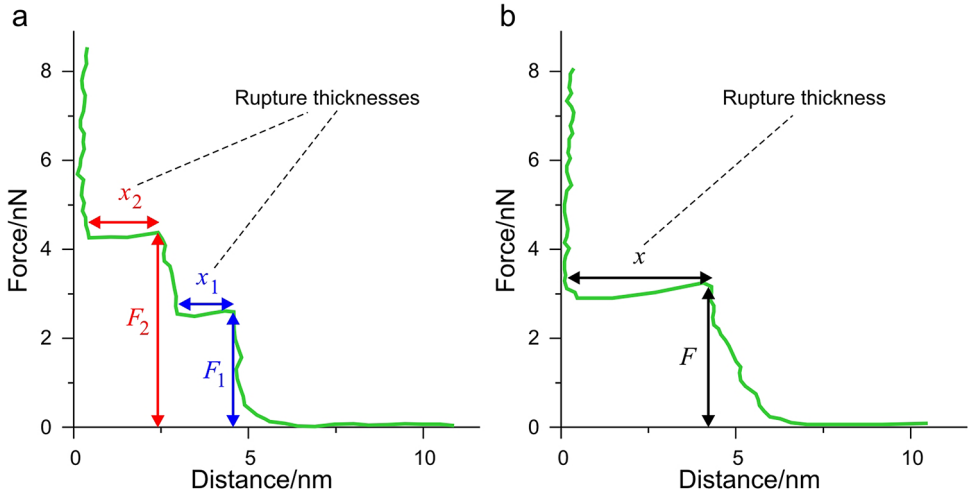

Fig. 3. Typical force-distance curves for demonstration while piercing through an SLB. (**a**) In most cases, the rupture of the bilayer consists of a sequential puncture through each of the layer. F_1 and F_2 mark these rupture forces, and x_1 and x_2 mark the layer thickness. (**b**) Some cases, the rupture of the bilayer can happen in one step, referred to as *complete rupture*.

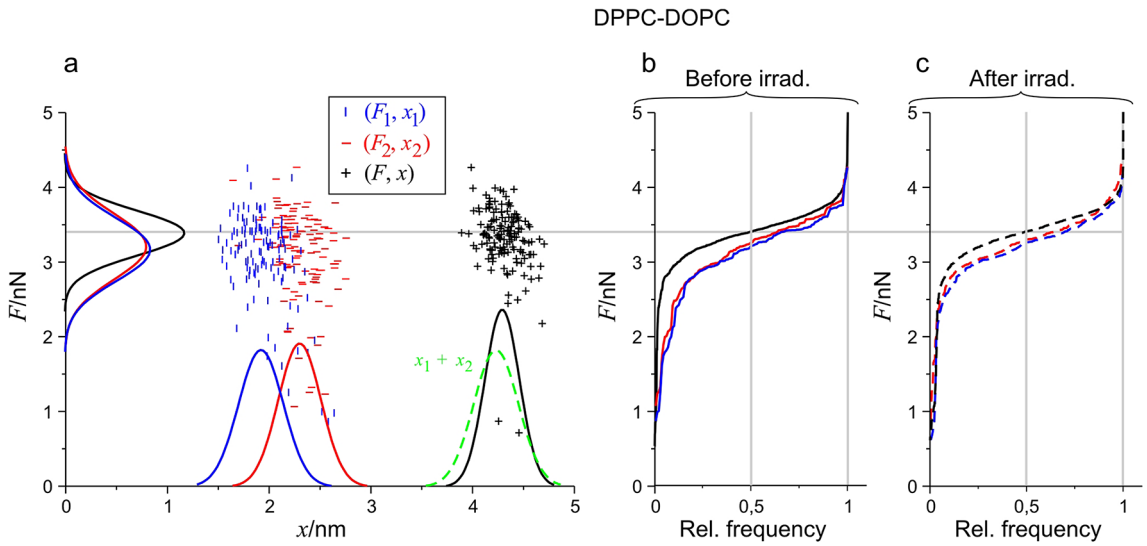

Fig. 4. Scatterplot and distribution of (F, x) data of every membrane rupture event for DPPC-DOPC sample. (**a**) 2D map of the distribution with fitted Gaussian density functions along the two axes blue color means the 1st, red means the 2nd, and black means the *complete rupture* event. The density function of the summation of respective rupture thicknesses $(x_1 + x_2)$ is also presented with a dashed green curve. (**b**) Cumulative distribution of F_1, F_2, and F with the same color codes with solid curves before irradiation. (**c**) Similar distributions are with dashed curves after irradiation. The grey line shows the median of *complete rupture* forces. $n = 1024$ for all data sets, but not every point is displayed in the scatterplot to avoid visual clutter.

the possibility of molecular changes and consequent alterations in membrane mechanics. To examine the effect of irradiation force, measurements were carried out on DPPC-DOPC SLBs before and after irradiation. To visualize and analyze the recorded data, rupture force and thickness values were displayed in an (F, x) scatter plot format that contained every membrane rupture event (Fig. 4a). We distinguished three different events: the 1st (F_1, x_1) corresponds to the events where the tip penetrated the first leaflet of the bilayer, the 2nd (F_2, x_2) marks the events where the tip penetrated the second bilayer leaflet. Lastly, (F, x) belongs to the events where the tip pierced through the bilayer in a single step (*complete rupture*). Cumulative distributions along both axes were generated from the data points of the scatter plots, and after derivation, the resulting density functions were fitted with the Gaussians.

In Fig. 4a, the fitted Gaussian of x displayed as a black curve along the horizontal axis, and dashed green for $x_1 + x_2$ overlaps almost completely. This means that rupture thickness is additive, that is if we add together

the average rupture thicknesses for x_1 and x_2, the resulting sum is in good agreement with the average rupture thickness of *complete ruptures*.

In Fig. 4b, and c, the cumulative distributions of the three force categories (F_1, F_2, F) are presented before and after irradiation. Noticeably, the median (relative frequency = 0.5; grey vertical line) of the F forces, represented as the solid and dashed black curves characteristic of the *complete rupture* appears the same both before and after irradiation. The medians of *individual rupture* forces (F_1, F_2; blue and red curves) remained unchanged. The distributions are practically identical, which indicate that no observable photoinduced alteration took place in the studied membrane system, in other words, there is no considerable irradiation-induced effect in DPPC-DOPC membranes in the absence of MPE.

Irradiation increases the stability of DPPC-DOPC-MPE membranes

The topography of photosensitized membranes (DPPC-DOPC-MPE) displayed drastic changes upon irradiation (Fig. 1b). To investigate the possible mechanical alterations, force measurements were carried out. Figure 5 shows the scatter plots of 1st and 2nd rupture events of a DPPC-DOPC-MPE SLB with the respective cumulative distributions for the rupture forces and density functions for rupture thicknesses before (Fig. 5a) and after (Fig. 5b) irradiation. *Complete ruptures* were rather scarce, thus they are not presented.

As each prepared membrane system is compared to itself during the experiments, the relative changes within a single experiment are a lot more reliable than the comparison of absolute values acquired from different experiments. Relatively large differences can occur in the absolute values of forces between different sets of experiments due to the deviation arising from cantilever calibration; furthermore, SLBs of different compositions are expected to have different mechanical properties. We can circumvent these errors by focusing on the relative changes of the subsequently measured forces, within a short time frame using the same cantilever[17]. The effect of irradiation on the mechanical properties of the photosensitized membrane is quite pronounced: both force distributions shifted towards higher values due to irradiation (Fig. 5b), while the decrease in x for the ruptures shows the thinning of the membrane. These alterations of the bilayer indicate pronounced alterations of the molecular interactions in the membrane.

Membrane disruption is mediated by unsaturated lipids

The AFM images showed that light-induced changes in the topography of photosensitized membranes could only be observed in the presence of unsaturated DOPC. However, this might conceal changes in the bilayer that do not alter the topography of the bilayer. Figure 6b presents the distribution of breakthrough forces of a DPPC bilayer containing MPE displayed as the DPPC-MPE sample. The saturated bilayer was unaffected by ROS formation as neither the average of F_1 or F_2 values nor the spread of the data changed before and after irradiation. By contrast, in DPPC-DOPC-MPE reference samples both F_1 and F_2 shifted towards higher values displaying higher stability after irradiation (Fig. 6a).

Direct and indirect effects in membrane alteration

Photosensitizers (PSs) can damage membranes in contact-dependent or independent manner[18,19]. In contact-dependent effects the excited PS comes into direct contact with the target to enable energy transfer between

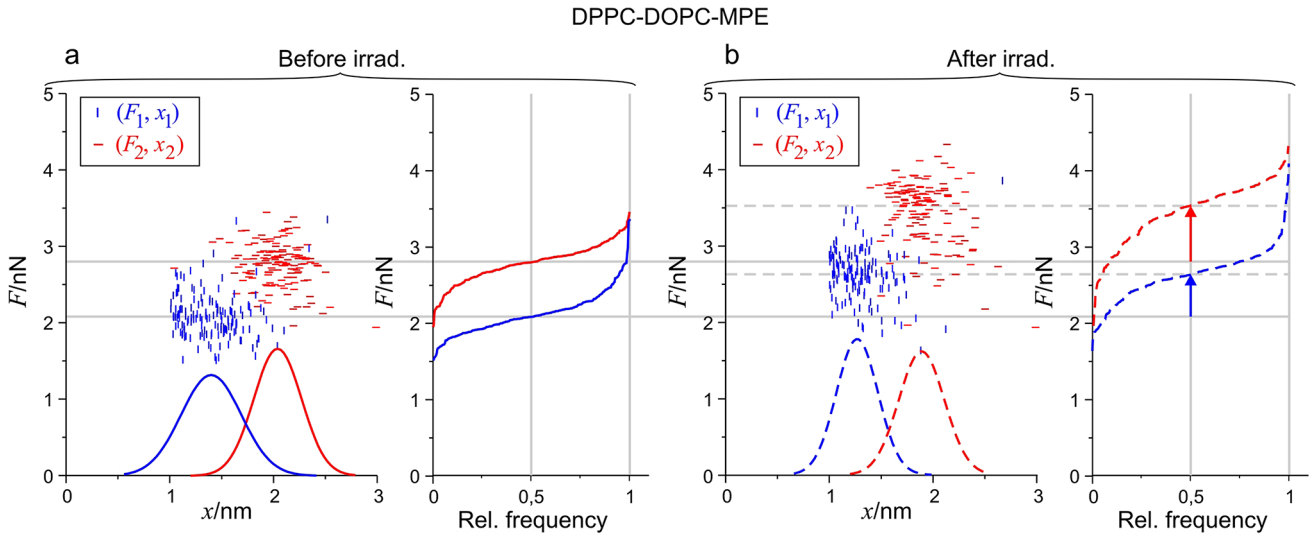

Fig. 5. Scatterplot and distribution of (F, x) data of the 1st and 2nd rupture events before and after irradiation for DPPC-DOPC-MPE SLB. (**a**) 2D maps of the distribution with fitted Gaussian density functions along the horizontal (x) axis. 1st rupture events are represented with blue, 2nd rupture events are represented with red, and the cumulative distribution of F1 and F2 are with the same color coding. (**b**) The same representation for the curves after irradiation the fitted curves are displayed with dashed lines. The arrows present the shift in the median F1 and F2 force due to irradiation.

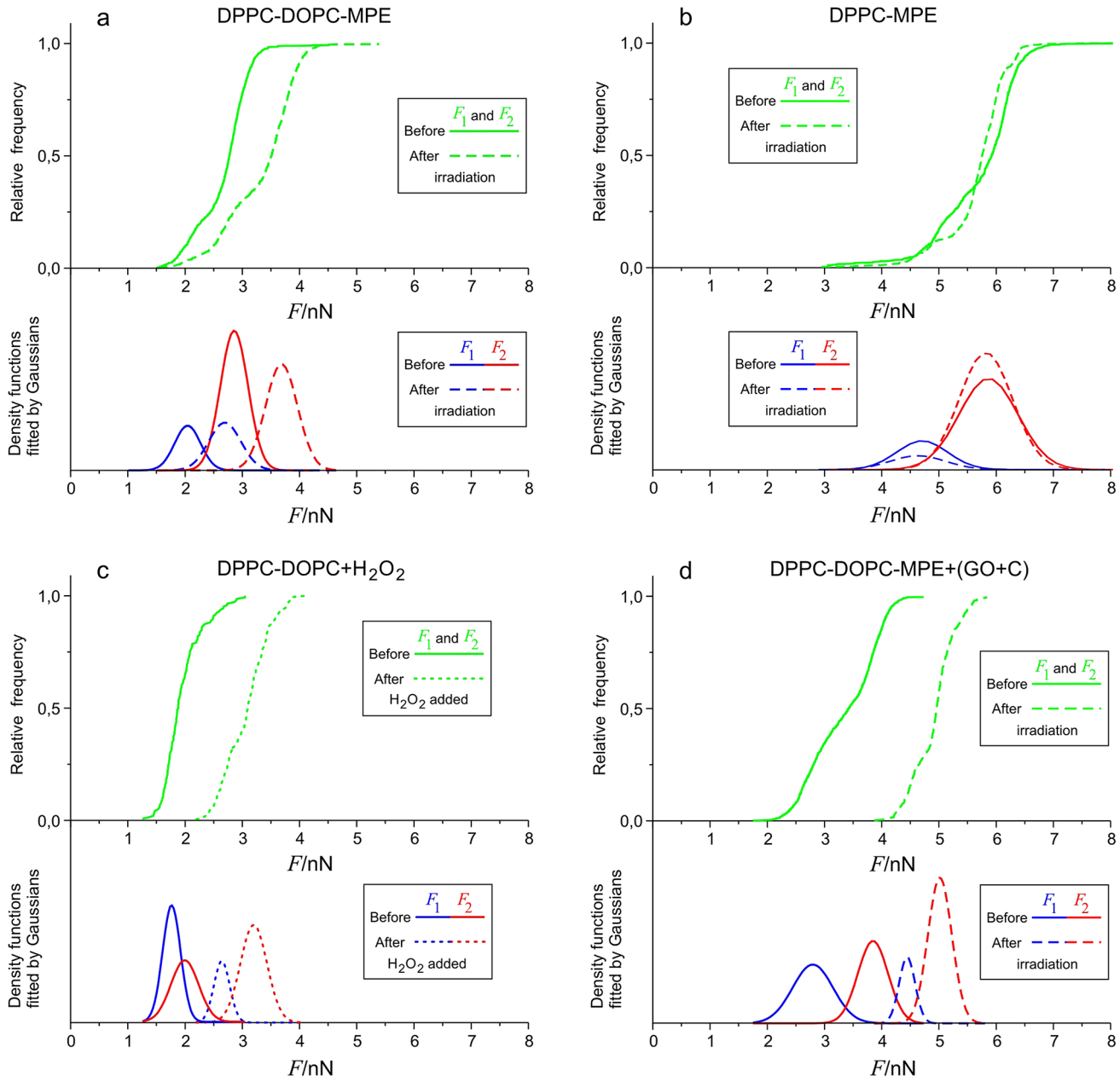

Fig. 6. Joint cumulative distribution functions of F1 and F2 forces and the individual components as Gaussian density functions for the four different samples before and after the treatment. (**a**) DPPC-DOPC-MPE as reference, (**b**) DPPC-MPE, (**c**) DPPC-DOPC(+H2O2), d) DPPC-DOPC-MPE(+GO+C). We used the same representation as before blue color means the F1, red means the F2 and green means F1 and F2 together. The functions displayed with a solid line represent the values before irradiation, the functions displayed with dashed lines represent the values after irradiation. Since the distribution for F1 and F2 overlap each other, a joint cumulative distribution function was produced from all the recorded breakthrough forces. From these curves, density functions were derived after smoothing and derivation. We then fitted the results as a decomposition of Gaussians. The components could be identified as separate F1 and F2 distributions. This figure compares the effects of the treatments on the indicated samples with the DPPC-DOPC-MPE sample.

them, whereas in the contact-independent case mediators are generated which then diffuse to the targets. These mediators are the different ROS. Figure 1d presents the topographical alterations in a bilayer treated with H_2O_2. The membrane integrity broke down, as holes emerged similarly to irradiated photosensitized membranes (Fig. 1b). To unveil whether similar nanomechanical alterations would emerge in the H_2O_2-treated bilayers as in the irradiated photosensitized membranes, we conducted force measurement on these membranes. The distribution of rupture forces recorded in DPPC-DOPC bilayers shifted towards higher values upon the addition of H_2O_2 (Fig. 6c) (DPPC-DOPC(+H_2O_2) sample), suggesting an increase in nanomechanical stability, just as it happened in the case of the DPPC-DOPC-MPE sample after irradiation. The results suggest that ROS formation

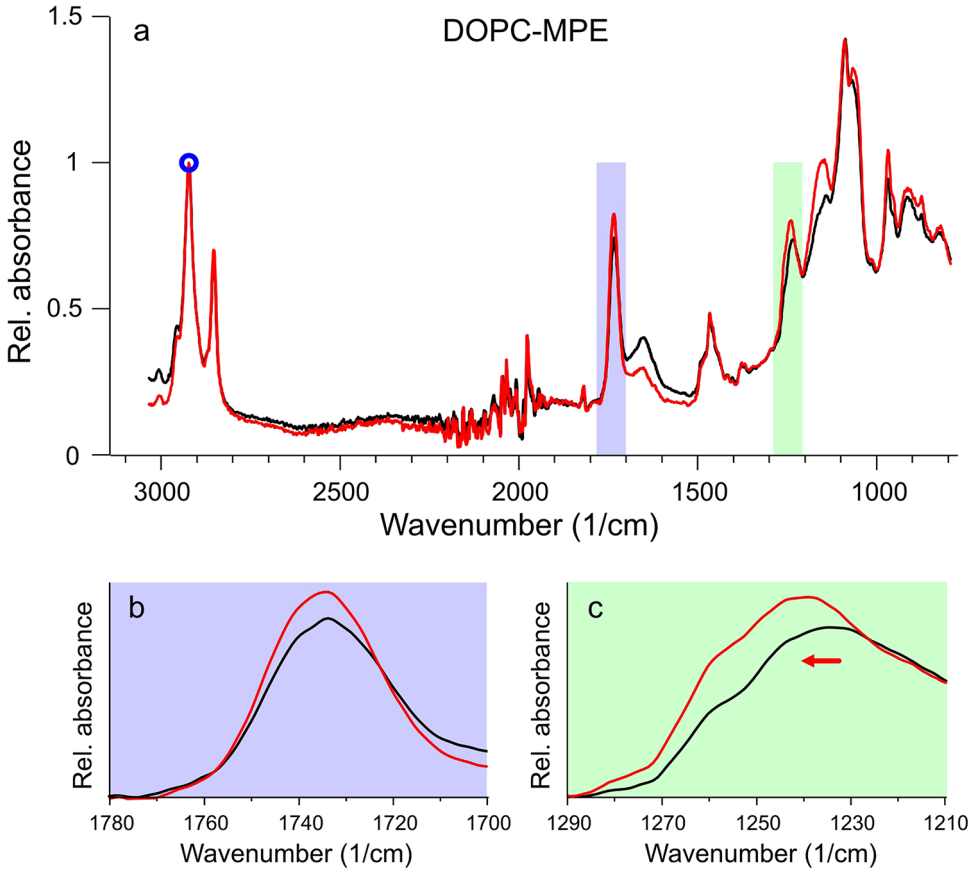

Fig. 7. FTIR spectra of DOPC-MPE sample. (**a**) The FTIR spectrum of DOPC-MPE vesicles before (black) and after (red) irradiation. A small blue circle indicates a characteristic lipid peak used for normalization. Lilac and green areas are enlarged below to present the characteristic spectral changes: the increased vas(C=O) peak (**b**), and the shifted and increased vas(PO2−) peak (**c**).

plays an important role in the molecular hence nanomechanical alterations of the membranes and highlights its contribution to hole formation.

Nevertheless, the contribution of contact-dependent reactions to membrane damage cannot be excluded either. To study the presence and importance of direct PS effects, we significantly reduced the oxygen concentration in our buffer in the DPPC-DOPC-MPE sample by adding GO + C to it (DPPC-DOPC-MPE(+ GO + C) sample). In lack of oxygen, ROS formation is essentially eliminated, and the observed effects are predominantly attributed to the direct effects of the PS molecules. For these experiments the DPPC-DOPC-MPE SLBs were prepared in glucose solution containing a high buffer capacity phosphate buffer to ensure that the added GO + C enzyme system does not alter the pH of the sample. This environment did not lead to perturbations in the topography of the SLB. Irradiation of these bilayers did not lead to hole formation in the bilayer. The distribution of rupture forces shifted towards higher values (Fig. 6d), which unequivocally indicates that contact dependent reactions alter the structure of the membranes significantly.

The chemical background of the detected topographical and nanomechanical changes

To investigate the chemical alterations that can lead to the topographical and nanomechanical changes in our model, we performed IR spectroscopy on photosensitized liposome solutions, before and after irradiation. First, we used the original DPPC-DOPC-MPE sample for this purpose, but alterations were barely apparent. Subsequently, DOPC-MPE liposomes were used for the experiment as our data showed that it is the unsaturated lipid and not DPPC that may be affected by photosensitization, leading to membrane hole formation.

The FTIR spectra (Fig. 7a) were normalized to a characteristic lipid peak, $\nu_{as}(CH_2)$ at about 2920 cm^{-1}, then compared to each other. Two considerable changes were observed and presented enlarged in Fig. 7bc panels. The $\nu_{as}(C=O)$ peak at 1735 cm^{-1} increased which is characteristic of oxidation of the membrane components[20], and the $\nu_{as}(PO_2^-)$ peak at around 1230 cm^{-1} shifted almost 10 cm^{-1} to the larger wavenumber values and increased in magnitude due to irradiation.

Discussion

Our results affirm that photosensitization can induce structural changes in the studied membrane models. Changes in the membrane structure due to photosensitization are shown in Fig. 1. It can be concluded that the

unsaturated lipid component has a fundamental part in the structural changes, since in membranes containing only saturated fatty acid chains, neither photosensitization nor the direct addition of ROS resulted in any change in the membrane structure. In the DPPC-DOPC membranes, both photosensitization and direct ROS addition resulted in hole formation by altering the distribution of breakthrough forces. Loss of membrane integrity was only observed in bilayers containing lipid components with unsaturated double bonds. Thus, the initial key process of hole formation should be the oxidation of unsaturated lipid components. The oxidation of the membrane components is supported by the change in IR spectra[21].

According to the currently accepted theory, the liquid-ordered state is rich in DPPC and the liquid-disordered state is mostly formed by DOPC in phase-separated DPPC-DOPC membranes. Based on this it would be logical to assume that the DOPC rich liquid-disordered state would be more prone to membrane damage. However, throughout our measurements, most of the holes were detected in the liquid-ordered phase and holes persisted within the liquid-ordered domain. We assume that hole formation within the membrane starts with a nucleation process. Accordingly, the lateral diffusion coefficient which is generally two magnitudes smaller within the liquid-ordered domains compared to the liquid-disordered domains[22] may allow nucleation sites to be stable long enough for stable structures to be formed by the incorporation of additional oxidized lipid molecules. Hence the environment of the liquid-ordered domain is more apt to produce lasting holes. The lack of holes in the liquid-disordered domain could be a consequence of the higher diffusion rate in this environment hindering the nucleation.

Lipids can form widely diverse structures; the formed structures depend on the packing parameter (*S*) of the lipids. Packing parameter is defined as.

$S = \frac{V}{a_0 l_c}$,

where V is the lipid chain volume, a_0 is the headgroup area, and l_c is the chain length[23]. Amphiphiles that form bilayers must have *S* greater than 0.5. The value of this parameter determines the type of formed aggregate. The corresponding *S* is 0.57 and 0.61 for DPPC and DOPC respectively[21]. This enables DPPC and DOPC to form vesicles in water as well as to form defect-free supported lipid bilayers on suitable substrate surfaces (Fig. 1ac).

To study the structural changes initiated by photosensitization, we have to understand the arising molecular changes induced by lipid oxidation. The target of the reaction is the unsaturated double bond present within the apolar tail region of the molecule. Through oxidation, a polar group is produced within the apolar lipid chain environment. These oxidized membrane lipids increase the headgroup area as the polar groups shift toward the polar headgroup region of the bilayer. These changes bring about the alteration of the critical packing shape of the oxidized lipids. The increase in packing parameters promotes the formation of inverted structures within the membrane such as holes, these holes produced within the membrane can be considered as inverted micelles within the membrane. Membrane breakthrough forces can be correlative with the ordering of membrane lipids. In its simplest form, the continuum nucleation theory describes the energy of a membrane hole with two physical parameters: the line tension (γ) representing the energy needed to create a unit length of hole boundary, and the surface tension (σ) which is proportional to the hole lumen area[24,25]. According to the model the energy of a hole can be expressed as:

$E(r) = 2\pi r\gamma - \pi r^2\sigma$.

Both of these parameters can be extracted from membrane breakthrough forces described by Robinsoon et al.[15]. In the presented model *P* is the probability of observing a membrane breakthrough event at force *F* with a constant loading rate which can be described by the following equations:

$$\ln P(F) = -\frac{A}{Kv}\int_{F_\sigma}^{F} \exp\left(-\frac{c}{F^* - F_\sigma}\right) dF^*$$

$$c = \frac{2\pi^2\gamma^2 R}{kT}$$

$$F_\sigma = 2\pi R\sigma.$$

A is the frequency of the attempted tip penetration which can be approximated by the resonance frequency of the cantilever. *K* is the spring constant of the cantilever, *υ* is the loading rate of the cantilever, *R* is the nominal tip radius of the tip, *k* is the Boltzmann constant and *T* is the temperature. Based on the integral, the γ and σ can be determined for the different force distributions as fit parameters[15,26,27].

For breakthrough force distributions in the DPPC-DOPC-MPE system, the line tension for the F_1 distribution was $\gamma = 12.55 \pm 0.61$ pN, whereas the F_1 distribution for the irradiated samples changed to $\gamma = 12.19 \pm 0.58$ pN. The surface tension was $\sigma = 14.84 \pm 0.05$ mN/m for before and $\sigma = 22{,}07 \pm 0.05$ mN/m after irradiation. For the F_2 distributions, the determined line tension was $\gamma = 12{,}55 \pm 0.61$ pN, after irradiation it changed to $\gamma = 13{,}57 \pm 0.69$ pN. While the surface tension for the F_2 distribution was $\sigma = 28{,}76 \pm 0.06$ mN/m before and $\sigma = 37{,}29 \pm 0.07$ mN/m after the irradiation.

The critical radius is a characteristic parameter, since the energy associated with this radius is the activation barrier for the formation of stable holes. This critical radius is.

$r_{crit} = \frac{\gamma}{\sigma}$

For both F_1 and F_2 distributions, the critical radius decreased after irradiation indicating an increased affinity toward hole formation. These parameters are in good agreement with previously reported values in the literature[23,26]. Based on the force curves of the liquid-ordered domains, the bilayer is more prone to hole formation after illumination, which is confirmed by imaging several membrane holes, observable in Fig. 1b, d.

Although for all the samples containing unsaturated fatty acids the membrane rupture force increased irrespectively from the type of the oxidative stress, the alterations were quite similar for the membranes treated with the direct addition of ROS and for the photosensitized membranes. Membrane breakthrough forces shifted to the higher values with a slight decrease in the breakthrough depth in both cases, and the previously continuous bilayer developed holes. In the presence of GO + C membrane integrity was preserved. GO converts

glucose to gluconic acid and hydrogen peroxide by using up the dissolved oxygen in the buffer environment. The enzyme cycle results in a net decrease of oxygen by consuming one oxygen molecule for the conversion of every two glucose molecules. By the addition of GO + C we could practically eliminate dissolved oxygen within the buffer[28]. For the type II reaction pathway for photosensitization dissolved oxygen is essential, since the first step for the reaction is an energy transfer between the excited photosensitizer and a triplet oxygen molecule[2]Σg) resulting in the formation of a much more reactive singlet oxygen[29]Δg)[30]. In this oxygen-depleted environment the type II reactions are hindered, giving way to type I reactions which are oxygen-independent. Due to photo-oxidation increased breakthrough forces and a slight decrease in the breakthrough depth occurred. This might be indirectly related to increased fraction of DPPC within the liquid-ordered domain[31].

Hole formation was captured through eight consequent frames shown in Fig. 2a. On the individual hole level, their fate is a mixed bag. Three colored circles highlight three different regions of interest: red, black and cyan. In the 2nd frame, two small holes are distinguishable within the red circle, in the 3rd frame the holes become more easily observable as both holes grow, one hole is significantly larger than the other, and then in the 4th frame, the two holes accrete. After accretion, the remaining hole kept increasing in radius throughout the following frames. There are two holes within the area marked by the black circle in the 2nd frame, and these have been steadily increasing throughout the frames then accreted to a single hole in frame seven and kept growing. The area marked by the cyan circle also has 2 circles in the 2nd frame. In the 3rd frame one of them has increased while the other has remained the same size, and in the 4th frame the smaller hole has disappeared completely while the other hole has increased in size and then disappeared by the 5th frame. These results show that a univocal description of the hole dynamics at the individual hole level is not possible.

Image analysis of AFM images allowed us to determine the size distribution of the holes. The Gaussians fitted to the measured points show that the newly formed holes are clearly smaller than the holes already present on the membrane. The sudden formation of the holes shows an exponential increase in the number of holes between the 2nd and the 3rd frame with a factor of 2.6. In the 2nd frame, only 10 holes were present, on the 3rd frame their number increased to 26, which further increased to 66 ($10 \times 2.6 = 26$; $26 \times 2.6 = 67.6$). Meanwhile, the total area covered by the holes showed a linear increase between frames 3 and 6, followed by a slight decrease at frames 7 and 8. To gain further insights into the evolution of membrane holes we studied all the present holes through eight consecutive images. Even though hole opening, closure, and accretion events, occurred simultaneously, the overall hole diameter kept increasing over time. As Fig. 2c shows the total area of the holes also increases up to the 6th frame, and between the 3rd and 6th frame the total area covered by the holes increased linearly with irradiation time. Meaning, that in this timeframe the total amount of oxidized lipids that take part in hole formation is proportional to the incoming photon number. In the case of the last two frames, some stabilization can be observed in this parameter. In addition, after the sudden burst of nucleation, the total area of the holes does not increase further, instead the hole diameter starts to increase as some holes close or coalesce while nucleation is still ongoing. Generally, this kind of process is called Ostwald ripening or coarsening. Growth of droplets by Ostwald ripening describes molecules diffusing through the solvent from the smaller to the larger particles. Thus, the larger particles will grow, and the smaller ones will shrink. During the reverse process of "dissolution", the system does not retrace the path it took during growth. For example, if the solution conditions are reversed at an intermediate stage, the droplets will dissolve back into the solvent, and each one will shrink. Several models exist for the description of Ostwald ripening[28,32], but a fully satisfactory approach has not yet been found, and it has remained a vexing problem in the field. Throughout our measurement, the local concentration of hole-forming lipid components exceeded the critical concentration required for nucleation, as below this threshold all holes would diminish in size simultaneously, which we did not observe during our experiments. As Oswald ripening is a diffusion-driven process, the slight increase in the total hole area might be due to the relative depletion of the hole-forming components within the diffusion range of the holes.

AFM imaging has provided further insights into the action of photodynamic processes leading to the loss of membrane barrier function. Our results present that the liquid-ordered domain is far more susceptible to hole formation than the liquid-disordered one. This indicates that different membrane domains can be specifically responsible for the loss of integrity from oxidative stresses.

Data Availability

The datasets used and analyzed during the current study available from the corresponding author on reasonable request.

Data availability

The datasets used and analysed during the current study available from the corresponding author on reasonable request.

Received: 30 July 2024; Accepted: 17 December 2024
Published online: 02 January 2025

References

1. Gao, Y., Yu, T., Zhang, Y., Dang, G. & Anti -VEGF Monotherapy Versus Photodynamic Therapy and Anti-VEGF Combination Treatment for Neovascular Age-Related Macular Degeneration: a Meta-analysis. *Invest. Ophthalmol. Vis. Sci.* **59**, 4307 (2018).
2. Elmets, C. A. et al. Joint American Academy of Dermatology–National Psoriasis Foundation guidelines of care for the management and treatment of psoriasis with phototherapy. *J. Am. Acad. Dermatol.* **81**, 775–804 (2019).
3. Houthoofd, S., Vuylsteke, M., Mordon, S. & Fourneau, I. Photodynamic therapy for atherosclerosis. The potential of indocyanine green. *Photodiagn. Photodyn. Ther.* **29**, 101568 (2020).
4. Ryskova, L., Buchta, V. & Slezak, R. Photodynamic antimicrobial therapy. *Open. Life Sci.* **5**, 400–406 (2010).

5. Sokolov, V. S. et al. Residence time of singlet oxygen in membranes. *Sci. Rep.* **8**, 14000 (2018).
6. Kim, J., Santos, O. A. & Park, J. H. Selective photosensitizer delivery into plasma membrane for effective photodynamic therapy. *J. Controlled Release*. **191**, 98–104 (2014).
7. Alves, E. et al. Overall biochemical changes in bacteria photosensitized with cationic porphyrins monitored by infrared spectroscopy. *Future Med. Chem*. **8**, 613–628 (2016).
8. Moisenovich, M. M. et al. Novel photosensitizers trigger Rapid Death of Malignant Human cells and Rodent Tumor Transplants via lipid photodamage and membrane permeabilization. *PLoS ONE*. **5**, e12717 (2010).
9. Johnson, G. A. et al. Photoinduced membrane damage of E. Coli and S. Aureus by the photosensitizer-antimicrobial peptide conjugate Eosin-(KLAKLAK)2. *PLoS ONE*. **9**, e91220 (2014).
10. Ytzhak, S., Weitman, H. & Ehrenberg, B. The effect of lipid composition on the permeability of fluorescent markers from Photosensitized membranes. *Photochem. Photobiol.* **89**, 619–624 (2013).
11. Herenyi, L. et al. Location of mesoporphyrin in liposomes determined by site-selective fluorescence spectroscopy. *J. Phys. Chem. B*. **113**, 7716–7724 (2009).
12. Veres, D. et al. Comparison of binding ability and location of two mesoporphyrin derivatives in liposomes explored with conventional and site-selective fluorescence spectroscopy. *J. Phys. Chem. B*. **116**, 9644–9652 (2012).
13. Bőcskei-Antal, B. et al. Comparison of light-induced formation of reactive oxygen species and the membrane destruction of two mesoporphyrin derivatives in liposomes. *Sci. Rep.* **9**, 11312 (2019).
14. Kiss, B. et al. Development, structure and mechanics of a synthetic E. Coli outer membrane model. *Nanoscale Adv.* **3**, 755–766 (2021).
15. Robinson, M., Filice, C. T., McRae, D. M. & Leonenko, Z. Atomic force microscopy and other scanning probe microscopy methods to study nanoscale domains in model lipid membranes. *Adv. Physics: X*. **8**, 2197623 (2023).
16. Attwood, S., Choi, Y. & Leonenko, Z. Preparation of DOPC and DPPC Supported Planar Lipid Bilayers for Atomic Force Microscopy and Atomic Force Spectroscopy. *IJMS* **14**, 3514–3539 (2013).
17. Frentrup, H. & Allen, M. S. Error in dynamic spring constant calibration of atomic force microscope probes due to nonuniform cantilevers. *Nanotechnology* **22**, 295703 (2011).
18. Bacellar, I. O. L. et al. Photosensitized membrane permeabilization requires contact-dependent reactions between Photosensitizer and lipids. *J. Am. Chem. Soc.* **140**, 9606–9615 (2018).
19. Bacellar, I. O. L. & Baptista, M. S. Mechanisms of photosensitized lipid oxidation and membrane permeabilization. *ACS Omega*. **4**, 21636–21646 (2019).
20. Oleszko, A. et al. Application of FTIR-ATR Spectroscopy to Determine the Extent of Lipid Peroxidation in Plasma during Haemodialysis. *BioMed Research International* 245607 (2015). (2015).
21. Jurak, M., Mroczka, R. & Łopucki, R. Properties of Artificial Phospholipid membranes containing lauryl gallate or cholesterol. *J. Membr. Biol.* **251**, 277–294 (2018).
22. Lindblom, G. & Orädd, G. Lipid lateral diffusion and membrane heterogeneity. *Biochim. et Biophys. Acta (BBA) - Biomembr.* **1788**, 234–244 (2009).
23. *Intermolecular and Surface Forces*. (Academic, Boston, (2011).
24. Cunill-Semanat, E. & Salgado, J. Spontaneous and stress-Induced pore formation in membranes: theory, experiments and simulations. *J. Membr. Biol.* **252**, 241–260 (2019).
25. Akimov, S. A. et al. Pore formation in lipid membrane I: continuous reversible trajectory from intact bilayer through hydrophobic defect to transversal pore. *Sci. Rep.* **7**, 12152 (2017).
26. Butt, H. J. & Franz, V. Rupture of molecular thin films observed in atomic force microscopy. I. Theory. *Phys. Rev. E*. **66**, 031601 (2002).
27. Loi, S., Sun, G., Franz, V. & Butt, H. J. Rupture of molecular thin films observed in atomic force microscopy. II. Experiment. *Phys. Rev. E Stat. Nonlin Soft Matter Phys.* **66**, 031602 (2002).
28. Baumann, R. P., Penketh, P. G., Seow, H. A., Shyam, K. & Sartorelli, A. C. Generation of oxygen deficiency in cell culture using a two-enzyme system to evaluate agents targeting hypoxic tumor cells. *Radiat. Res.* **170**, 651–660 (2008).
29. Kurokawa, H., Ito, H. & Matsui, H. Porphylipoprotein Accumulation and Porphylipoprotein Photodynamic Therapy effects Involving Cancer cell-specific cytotoxicity. *IJMS* **22**, 7306 (2021).
30. Baptista, M. S., Cadet, J., Greer, A. & Thomas, A. H. Photosensitization reactions of Biomolecules: definition, targets and mechanisms. *Photochem. Photobiology*. **97**, 1456–1483 (2021).
31. Maekawa, T. et al. Molecular diffusion and nano-mechanical properties of multi-phase supported lipid bilayers. *Phys. Chem. Chem. Phys.* **21**, 16686–16693 (2019).
32. Baldan, A. Review progress in Ostwald ripening theories and their applications to nickel-base superalloys part I: Ostwald ripening theories. *J. Mater. Sci.* **37**, 2171–2202 (2002).

Acknowledgements

TKP2021-EGA-23 has been implemented with the support provided by the Ministry of Innovation and Technology of Hungary from the National Research, Development and Innovation Fund. Bálint Kiss was supported by the EKÖP-24-85 university excellence scholarship program of the Hungarian Ministry for Culture and Innovation from the source of the National Research, Development and Innovation Fund.

Author contributions

Á.Z. designed research, performed experiments, analysed data, wrote the manuscript; B.K. and T. B. helped to perform experiments, contributed during the writing process; J. S. performed and analyzed FTIR experiments; I. V. helped in mathematical analyses of data; M.K. performed and analysed AFM experiments, corrected the manuscript; L.H. designed research, conceived experiments, analysed the results, prepared figures, wrote the manuscript.

Declarations

Competing interests

The authors declare no competing interests.

Additional information

Correspondence and requests for materials should be addressed to L.H.